Available online at www.sciencedirect.com
SciVerse ScienceDirect
Ceramics International 39 (2013) 4221–4230
CERAMICS INTERNATIONAL
www.elsevier.com/locate/ceramint

Structural, magnetic, electrical and dielectric properties of $Mn_xNi_{1-x}Fe_2O_4$ spinel nanoferrites prepared by PEG assisted hydrothermal method

Yüksel Köseoğlu*

Department of Physics, Fatih University, Buyukcekmece, 34500 Istanbul, Turkey

Received 1 October 2012; received in revised form 15 October 2012; accepted 2 November 2012
Available online 10 November 2012

Abstract

$Mn_xNi_{1-x}Fe_2O_4$ ($x=0.2$, 0.4, 0.6) nanoparticles were synthesized by a polyethylene glycol (PEG)-assisted hydrothermal route. We present a systematic investigation on the structural, magnetic, electrical and dielectric properties of the products by using XRD, FT-IR, SEM, TGA, VSM and dielectric spectroscopy, respectively. Single phased cubic spinel structure was confirmed for all samples and the average crystallite size of the products was estimated using Line profile fitting and ranges between 6.5 and 11 nm. The nanoparticles have ferromagnetic nature with small coercivity. The samples showed semiconducting behavior which is revealed from temperature dependent conductivity measurements. Temperature and frequency dependent dielectric property; dielectric permittivity (ε) and ac conductivity (σ_{AC}) studies for the samples indicated that the dielectric dispersion curve for all samples showed usual dielectric dispersion confirming the thermally activated relaxation typical for Debye-like relaxation referring to it as the Maxwell–Wagner relaxation for the interfacial polarization of homogeneous double structure. The particle size, saturation magnetization, coercive field, conductivity and dielectric constant of the samples are strictly temperature dependent and increased with Mn concentration.

Keywords: Hydrothermal synthesis; Magnetic nanomaterials; Spinel ferrites; Magnetic semiconductor

1. Introduction

Spinel ferrite nanoparticles have attracted considerable interest and efforts of scientists and engineers to investigate their magnetic, electrical, dielectric and catalytic properties for their technological applications in the industries as inductive and capacitive materials, microwave absorbers, disk recording, refrigeration systems, electrical devices, ferrofluids, etc. The spinel structure allows the introduction of different metallic ions without changing the spinel crystal structure and there is a possibility of achieving control over the structural, magnetic, electrical and dielectric properties of spinel ferrites by substitution of M^{2+} ions (Me=Co, Mn, Ni, Zn, etc.) [1–7].

Spinel ferrites have the general structure of $[M^{2+}]_{tet}[Fe^{3+}]_{octa}O_4$ and the introduction of third metal ion modifies the distribution of ions in the spinel structure. The distribution of Fe^{3+} and M^{2+} ions can easily be altered by simply varying the concentration of third metal ion which results the manipulation of their magnetic, electrical, dielectric and catalytic properties [8–12].

Mn-ferrite has mostly normal type spinel structure. Ni-ferrite has a fully inverse type spinel structure contrary to Mn-ferrite. $NiFe_2O_4$ exhibits ferrimagnetic behavior originating from magnetic moments of antiparallel spins between Fe^{3+} ions at the tetrahedral sites and Ni^{2+} ions at the octahedral sites of the spinel structure [13–16]. Considering this, Ni–Mn ferrites present interesting compositions and physical properties to investigate. They are a kind of soft magnetic materials with low coercivity that is both to get and loss magnetization [17,18]. The substitution of Mn^{2+} ions in Ni-ferrites lead to the modification of the structural, magnetic, electrical and dielectric properties.

To the best of our knowledge, there is relatively less of work to describe the magnetic, electrical and dielectric

---

*Fax: +90 212 8663402.
E-mail address: yukselk@fatih.edu.tr

0272-8842/$ - see front matter © 2012 Elsevier Ltd and Techna Group S.r.l. All rights reserved.
http://dx.doi.org/10.1016/j.ceramint.2012.11.004

properties of this important class of $Mn_xNi_{1-x}Fe_2O_4$ nanoferrites. In this study, we aim to prepare Mn substituted Ni ferrite nanoparticles with a low sintering temperature involving less energy and low cost metal nitrates as raw materials by using polyethylene glycol (PEG) assisted hydrothermal method which is cheap and easy to get a good result. The method of hydrothermal synthesis is processing at high pressure and low temperature at around 180 °C. It can be defined as any homogeneous (nanoparticles) or heterogeneous (bulk materials) reaction in the presence of aqueous solvents or mineralizers under high pressure and low temperature conditions to dissolve and recrystallize (recover) materials that are relatively insoluble under ordinary conditions [19–21]. During the synthesis we used low-cost coating material PEG as the surfactant which is one of the polymers with major interest in this area because it is non-toxic, non-flammable and easy to handle. Various morphologies with different sizes and shapes can be obtained by PEG-coating. It is verified that using PEG is very advantageous to prevent agglomerations and to obtain small particle sizes with good crystallinity as emphasized in different works [19–21].

2. Experimental

2.1. Synthesis

To prepare Mn–Ni ferrite ($Mn_xNi_{1-x}Fe_2O_4$) nanoparticles (NPs) (with $x=0.2$, 0.4, 0.6), stoichiometric molar amounts of nickel nitrate [$Ni(NO_3)_2 \cdot 6H_2O$], ferric nitrate [$Fe(NO_3)_3 \cdot 9H_2O$], and manganese nitrate [$Mn(NO_3)_2 \cdot 6H_2O$] were each dissolved in 10 mL of distilled water to form a clear solution and mixed altogether. The mixture was stirred with a magnetic stirrer until the reactants were dissolved completely. During the stirring, 10 ml PEG-400 was added to the solution to serve as surfactant that covers NPs and prevents agglomeration. And pH of the solution was adjusted to 11.0 by adding 2 M NaOH as drop wise during stirring. After continuous stirring at 400 rpm for an hour, a homogeneous solution could be obtained. The obtained solutions were put into the autoclaves up to two thirds of their total volume (50 mL). The autoclaves were kept at 150 °C for 12 h, then were allowed to cool to room temperature. The products were centrifuged and washed several times with de-ionized water, acetone and absolute ethanol. Then the samples were put again in an oven at 70 °C to dry. Taken solid phase samples were grinded in a mortar to make them powder and were used for all of the measurements.

2.2. Measurements

X-ray powder diffraction (XRD) analysis was conducted on a Rigaku Smart Lab Diffractometer operated at 40 kV and 35 mA using Cu K_α radiation.

FTIR transmission spectra were taken on Mattson Satellite Infrared Spectrometer from 4000 to 400 cm^{-1} in order to investigate the nature of the chemical bonds formed.

Field Emission Scanning Electron Microscope (FE-SEM, JEOL 7001 FE) was used in order to investigate the nanostructure and morphology of the samples. Samples were coated with carbon prior to SEM analysis.

The thermal stability was determined by thermogravimetric analysis (TGA, Perkin Elmer Instruments model, STA 6000). The TGA thermograms were recorded for 5 mg of powder sample at a heating rate of 10 °C/min in the temperature range of 30 °C–800 °C under nitrogen atmosphere.

VSM measurements were performed by using a Quantum Design Vibrating sample magnetometer (QD-VSM). The samples were measured between ±10 kOe at room temperature and 10 K. ZFC (zero field cooling) and FC (field cooling) measurements were carried out at 50 Oe and the blocking temperature was determined from the measurements.

Conductivity (ac–dc) and dielectric measurements of the products were studied by Novocontrol dielectric spectroscopy in the range 20–120 °C with a step of 10 °C (frequency range 0.1 Hz–3 MHz).

3. Results and discussion

3.1. XRD analysis

XRD studies of products confirmed the formation of single phase cubic spinel structures. Typical XRD patterns of $Mn_xNi_{1-x}Fe_2O_4$ system is presented in Fig. 1. All of the observed diffraction peaks are indexed by the cubic structure of $NiFe_2O_4$ (JCPDS no. 19-629). The average crystallite sizes were calculated by Scherer's equation (Eq. (1)) from the reflection of the spinel structure's $d_{(311)}$ plane.

$$D_{XRD} = 0.9\lambda / \{\beta \cos\theta\} \qquad (1)$$

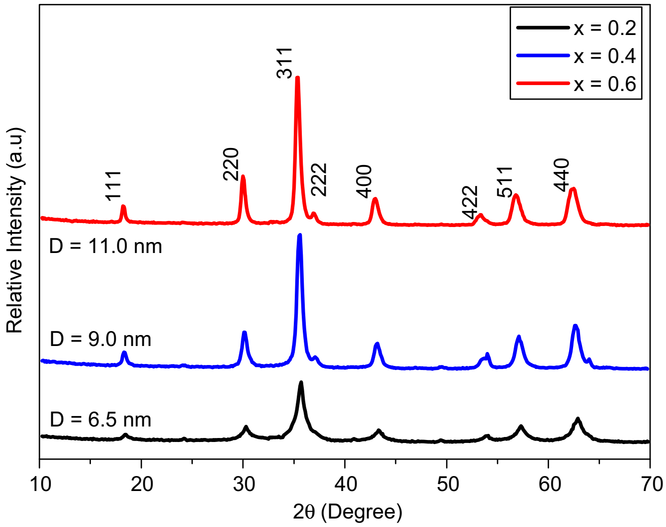

Fig. 1. XRD pattern of $Mn_xNi_{1-x}Fe_2O_4$ NP's synthesized by PEG-assisted hydrothermal method.

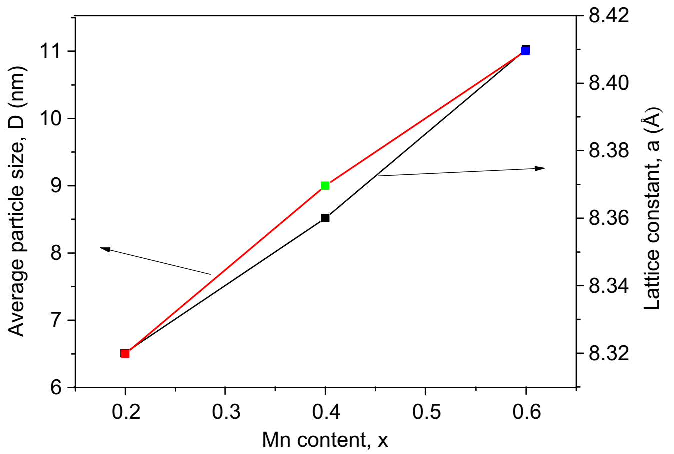

Fig. 2. Variation of average particle size and the lattice parameter as a function of Mn content.

Here, D_{XRD} stands for crystallite size; λ is the wavelength of the radiation and β is the full width at half maximum (in radians) centered at 2θ of the most intense peak (in this case it is the peak of [311]) [19–21]. The calculated sizes of the particles are found to be ranging between 6.5 and 11 nm.

The accurate values for lattice parameters "a" have been calculated from main diffraction peak of each sample using the d-spacing values and the respective (h k l) parameters by using the classical Nelson–Riley formula given as:

$$a = 1/2\left(h^2 + k^2 + l^2\right)/\sin\theta \tag{2}$$

The crystallite sizes and lattice parameters are found to increase almost linearly by increasing Mn content (see Fig. 2) which is obeying Vegard's law [22,19] as shown in Fig. 2. These can be attributed to the difference in sizes of the ionic radii that is the ionic radius of Mn^{2+} (Tet: 0.655 Å; Oct 0.80 Å) is relatively greater than the ionic radius of Ni^{2+} (Tet: 0.55 Å; Oct: 0.69 Å) [23,24]. The increase of crystal size and lattice constant with increase in x is because of the fact that the smaller ionic radii of Ni^{2+} are replaced by larger ionic radii of Mn^{2+}. The replacement of nickel ion by manganese ion caused an increase in the interatomic spacing parameter 'd' and consequently lattice parameter increased in accordance with the Vegard's law [23,24]. These results found are in good agreement with several other studies where smaller metal ions have been substituted with relatively larger metal ions [8,21,25–28].

3.2. SEM analysis

Fig. 3 shows field emission scanning electron micrographs (FE-SEM) of $Mn_xNi_{1-x}Fe_2O_4$ system. As seen from SEM pictures the samples consist of almost spherical shaped NPs with the existence of soft agglomeration. They also reveal that samples have smaller crystallites with sizes at around 50 nm (see Fig. 3). Nanoparticles were dense and distributed regularly on the whole area. In addition to this, although these smaller crystallites are so closely arranged together, a clear boundary between neighboring crystallites can yet be observed. The larger particle sizes of the NPs can be attributed surfactant (the PEG coating) on the surface of the nanoparticles which does not count in crystallite sizes since PEG is amorphous [25].

3.3. FT-IR analysis

The room temperature IR spectra of as prepared samples and polyethylene glycol (PEG) are shown in Fig. 4. From IR spectra of all spinels and ferrites two main broad metal-oxygen bands can be observed in particular. The highest IR band-υ_1, (Fig. 3) generally observed in the range 600–550 cm^{-1}, corresponds to intrinsic stretching vibrations of the metal at the tetrahedral site, $M_{tetra} \leftrightarrow O$, whereas the lowest IR band-υ_2, usually observed in the range 450–385 cm^{-1}, is assigned to octahedral-metal stretching, $M_{octa} \leftrightarrow O$ [15,29,30]. In Fig. 4, the bands observed between 580 and 600 cm^{-1} correspond to stretching vibrations of tetrahedrally coordinated metal-oxygen bonds, and the bands observed at around 420 cm^{-1} corresponds to stretching vibrations of octahedrally coordinated metal-oxygen bonds. It is known that Ni^{2+} ions have octahedral-site preference, while Mn^{2+} and Fe^{3+} ions can occupy both octahedral and tetrahedral sites [29]. The observed bands υ_1 and υ_2 are characteristics of MnNi ferrites as reported elsewhere [29].

3.4. Thermal analysis

Thermal stability of $Mn_xNi_{1-x}Fe_2O_4$ NP's and PEG has been analyzed using TGA (Fig. 5). TGA was performed in the temperature range of 30–700 °C to further confirm the existence of PEG on the surface of $Mn_xNi_{1-x}Fe_2O_4$ nanoparticles and quantify the proportion of organic and inorganic phases. Pure PEG has started to combust at ~330 °C and completely combusted at ~425 °C [19,31]. Evidently, the combustion of PEG coated $Mn_xNi_{1-x}Fe_2O_4$ nanoparticles starts earlier than the decomposition of pure PEG and continues up to 700 °C. The earlier part of combustion curve is due to the evaporation of organic solvents and water. The second part (between 230 and 425 °C) corresponds to decomposition of PEG and $Mn_xNi_{1-x}Fe_2O_4$ composites into oxides. The temperature at which the decomposition of PEG coated $Mn_xNi_{1-x}Fe_2O_4$ nanoparticles starts is lower than that of PEG alone, which indicates the catalytic effect of $Mn_xNi_{1-x}Fe_2O_4$ nanoparticles on the degradation of the PEG [32,33]. Nanocomposites show a major weight loss of ~15% over the temperature range of 30–700 °C due to the decomposition and combustion of PEG. This implies that nanocomposites have ~85% inorganic phase as $Mn_xNi_{1-x}Fe_2O_4$ nanoparticles.

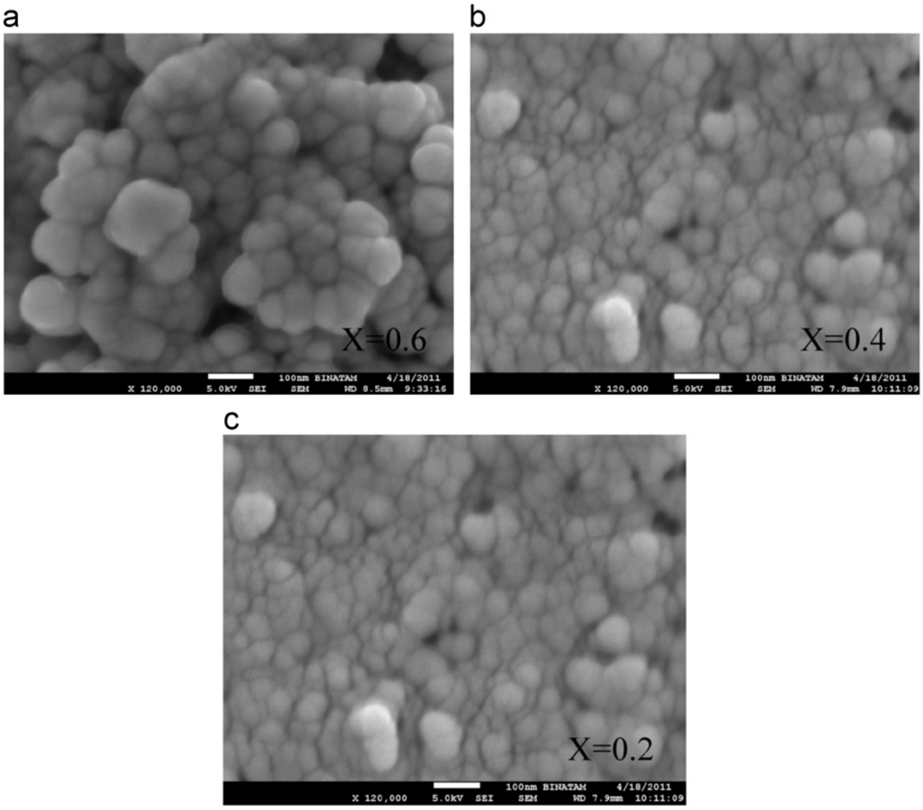

Fig. 3. SEM pictures of $Mn_xNi_{1-x}Fe_2O_4$ NPs synthesized by PEG-assisted hydrothermal method.

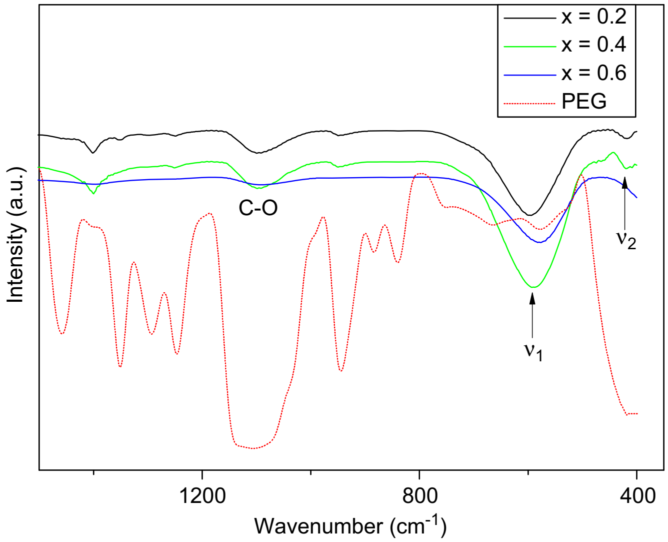

Fig. 4. FTIR spectra of $Mn_xNi_{1-x}Fe_2O_4$ NP's and PEG.

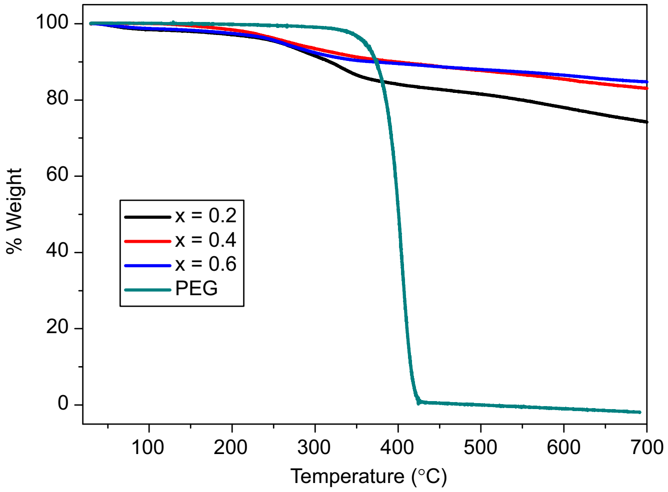

Fig. 5. TGA thermograms of $Mn_xNi_{1-x}Fe_2O_4$ NP's and PEG.

3.5. *Magnetic measurements*

Variation of magnetization M (emu/g) with the applied field H (Oe) (M–H loops at room temperature and at 10 K for the prepared $Mn_xNi_{1-x}Fe_2O_4$ NPs are shown in Fig. 6. At room temperature, the narrow loops for all the samples showing almost no hysteretic behavior indicate the soft nature of the $Mn_xNi_{1-x}Fe_2O_4$ NPs. The zero coercivity and sharp increase in the magnetization of the samples with the applied field indicate the superparamagnetic nature of the samples. The magnetization of the samples also increases with the Mn concentration. At 10 K, the M–H curves have hysteretic behavior indicating the ferromagnetic behavior of the samples at low temperatures. The magnetization and the coercivity of the samples increased relative to room temperature values. The coercivity (H_c) is generally a measure of magneto-crystalline anisotropy for

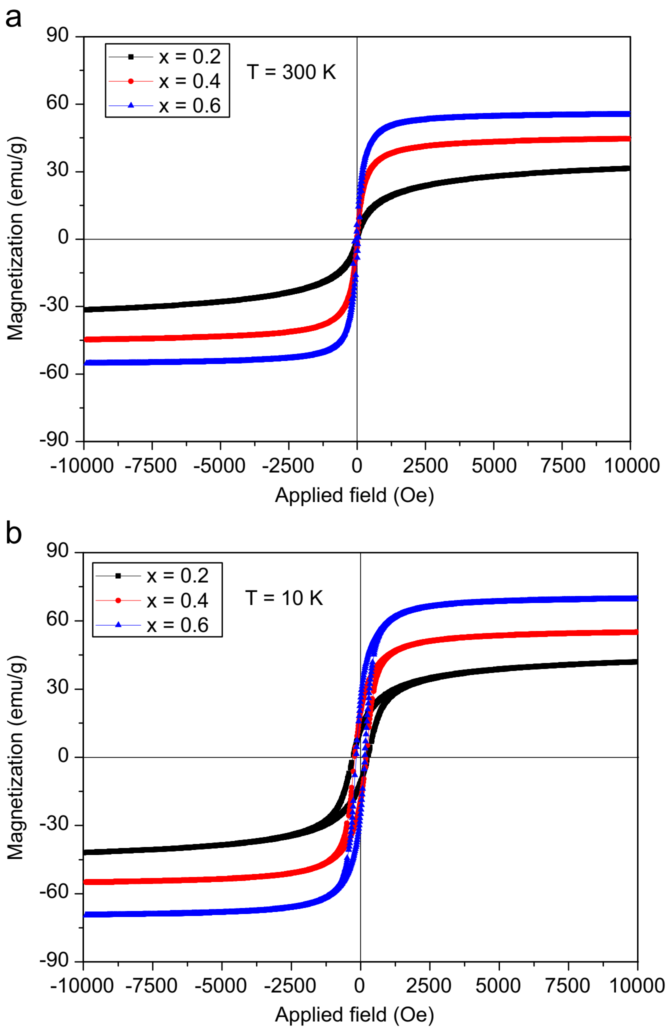

Fig. 6. M–H loops of $Mn_xNi_{1-x}Fe_2O_4$ NP's (a) at room temperature and (b) at 10 K.

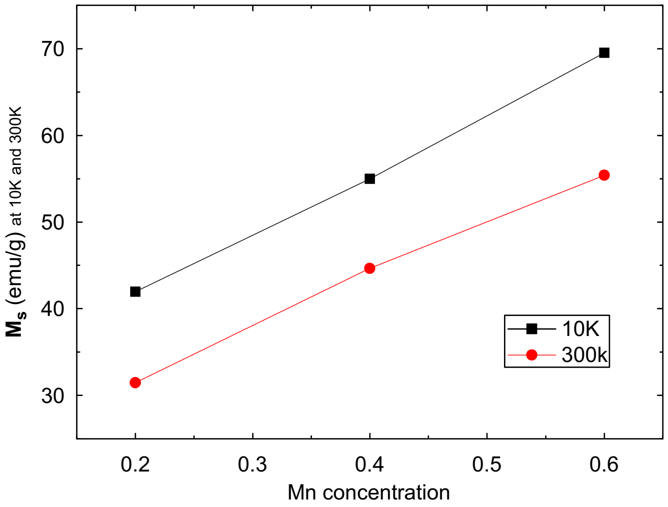

Fig. 7. Variation of saturation magnetization, Ms with Mn content.

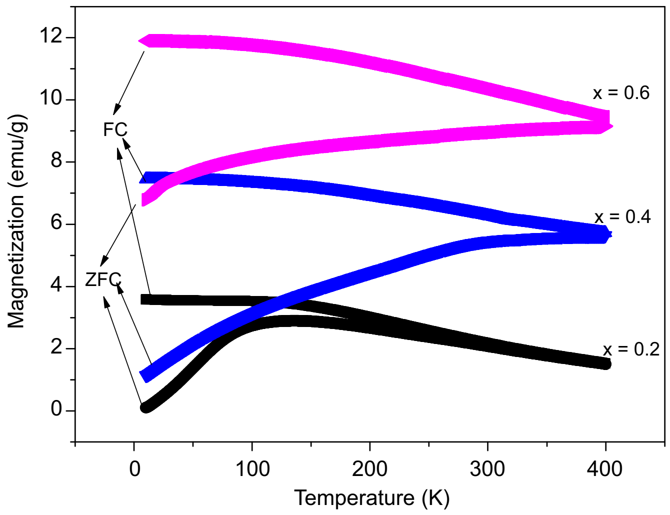

Fig. 8. Temperature variation of magnetization of $Mn_xNi_{1-x}Fe_2O_4$ NP's with 50 Oe applied field.

a magnetic material but it may also originate from exchange anisotropy due to spin disorder at the particle surface at low temperatures [15,16]. At all temperatures, the M–H curves of $Mn_xNi_{1-x}Fe_2O_4$ NPs do not reach complete saturation even at 10 kOe applied magnetic field. This behavior is often observed in nanoparticles and can be attributed to the presence of a spin disordered surface layer which requires a larger field to be saturated together with the concomitant effect of small size of the nanoparticles with not too much anisotropy [9]. Also a small fraction of them are still fast relaxing at 10 kOe.

The saturation magnetizations (obtained from the linear extrapolation of M vs. 1/H) of $Mn_xNi_{1-x}Fe_2O_4$ NPs are found between 31 and 56 emu/g at room temperature and 41–70 emu/g at 10 K. The obtained values of saturation magnetization for $Mn_xNi_{1-x}Fe_2O_4$ NPs are lower than the saturation magnetization of bulk Mn-ferrite (Ms = 110 emu/g) and of bulk Ni-ferrite (Ms = 55 emu/g) [7,19,34]. This can be attributed to the surface effects for nanosized materials. Variation of saturation magnetization with the Mn content is shown in Fig. 7. The saturation magnetization of the samples is increasing with Mn content and larger than the value obtained for $x = 0.2$ sample [19]. This can be attributed to larger magnetic moments of Mn ions (5 μ_B) substituted with Ni ions having smaller magnetic moments of 2.83 μ_B at the octahedral site [7,19,34]. The absence of saturation and coercivity even at an applied field of 10 kOe indicates the presence of superparamagnetic single domain nanoparticles [35,36].

The temperature dependence of the zero field cooled (ZFC) and field cooled (FC) magnetizations measured with 50 Oe applied field are shown in Fig. 8. The ZFC magnetization curve exhibits the typical features of an assembly of magnetic nanoparticles with a distribution of blocking temperature. This property is characterized by the relatively broad cusp at some temperatures corresponding to the blocking temperature, T_B, indicating that the magnetic moment of each particle becomes blocked in the direction determined by its easy magnetization axis at a given temperature T_B. The temperature dependent magnetization of $Mn_xNi_{1-x}Fe_2O_4$ NP's increases by decreasing the temperature and ZFC curve for $Mn_xNi_{1-x}Fe_2O_4$ sample exhibits a relatively broad cusp at some temperatures corresponding to the blocking temperature, T_B of the samples [5,6,8,15]. Then ZFC magnetization decreases by decreasing the temperature. The blocking temperature of the samples is increased with Mn content from 135 K for $x=0.2$ [19] to 375 K for $x=0.4$ and 400 K for $x=0.6$, respectively. The samples with higher Mn content ($x=0.4$ and 0.6) having blocking temperatures above the room temperature indicate that these samples behave ferromagnetic below the room temperature and superparamagnetic above the blocking temperature. The broad cusp in ZFC magnetization curve indicates the existence of different sized nanoparticles having different blocking temperatures [15,16,19,21]. Because the particles in the samples have a certain distribution of volumes, each of them becomes blocked at different temperatures, giving rise to a distribution of blocking temperature and observation of a broad peak in the ZFC magnetization curve. The FC magnetization increases with decreasing temperature as expected and tends to saturate at very low temperatures as seen in Fig. 8.

Decreasing the size of the magnetic materials to nanometer dimensions leads to unique effects like superparamagnetism, enhanced magnetization relative to bulk and (below a critical dimension) single domain magnetic nanoparticles as seen for $Mn_{0.2}Ni_{0.8}Fe_2O_4$ [19]. These fine particles exhibit single domain ferromagnetism below the blocking temperature, T_B, and superparamagnetism above T_B. The moment of each nanoparticle freely rotates in the superparamagnetic state, so a collection of nanoparticles acts like a paramagnet where the constituent moments are ferromagnetic nanoparticles (rather than atomic moments as in a normal paramagnet).

Below the blocking temperature T_B, the FC and ZFC magnetization curves significantly diverge and $Mn_xNi_{1-x}Fe_2O_4$ NP's are in ferromagnetic state. Above T_B, The FC and ZFC curves coincide due to the fact that all nanoparticles are at the superparamagnetic state. Below T_B, particle's moment appears to be blocked with respect to the time scale of the experiment and the magnetic moments of the particles are magnetically frozen along their anisotropy axes. The superparamagnetic particles deflect uniquely to the strong field side of the gradient magnet, but this effect decreases as a function of increasing temperature. At the blocking temperature, the thermal fluctuation energy (k_BT) comparable to the energy barrier for the magnetic moment reversal associated with the total anisotropy energy ($E_A=MVH$). At the temperatures higher than T_B, the single particle's moment progressively unblocks and superparamagnetic moment of particles becomes thermally unstable and magnetizations exponentially decrease as MVH/k_BT becomes smaller than 1. Above the blocking temperature T_B, the thermal fluctuation energy (k_BT) is larger than the uniaxial anisotropy energy (KV), because the critical volume for nanoparticles behaving as a single domain is larger than the studied magnetic particle's volume [5,6,19,37]. At high temperature regime, assuming an equilibrium state, the magnetic susceptibility follows a Curie–Weiss law [19,38] with a ferromagnetic transition temperature Tc. The magnetic state for $T>T_B$ is called as superparamagnetic state in which the remanence and coercivity of the system vanish.

For ZFC and FC measurements, at the blocking temperature, it is usually assumed that

$$K_{eff}V = 25k_BT_B \tag{3}$$

where K_{eff} is the effective anisotropy constant including all of the different anisotropies contributing to the effective anisotropy (such as the magnetocrystalline, shape, surface and stress magnetic anisotropies), V is the average volume of the nanoparticles, k_B is the Boltzmann constant and T_B is the blocking temperature of the nanoparticles. By using Eq. (3), K_{eff} values can roughly be determined by considering the particles mean size D as determined by Sherrer analysis. K_{eff} values for $Mn_xNi_{1-x}Fe_2O_4$ NP's are found as 3.25×10^6, 3.40×10^6 and 1.99×10^6 erg/cm^3 for $x=0.2$, $x=0.4$ and $x=0.6$ samples, respectively. All of these values are much higher than those found for bulk samples of $MnFe_2O_4$ and $NiFe_2O_4$ (0.025×10^6 and 0.07×10^6 erg/cm^3, respectively) [9], as expected for nanosized particles, where high surface anisotropy plays an active role in increasing the total anisotropy. K_{eff} values found for our samples seem to be greater than those found by Carta et al. [9]. These differences can be attributed to the presence of dipolar and/or exchange interactions among the particles. Such kinds of interactions are well-known to increase to increase with the volume of the particles and to decrease with the mean distance among them.

As a result, the magnetization of the $Mn_xNi_{1-x}Fe_2O_4$ NPs has superparamagnetic nature at around the room temperature and ferromagnetic nature below the blocking temperature. The decrease in magnetization below the blocking temperature should be attributed to spin frustration in spin-glass like phase which may be thought of for the random distribution of magnetic dipoles. This spin frustration is consistent with the spin-canting due to the decrease in effective super-exchange interactions among magnetic spins at the surface regions reflecting itself as a decrease of average magnetization of single domain particle as mentioned above [19].

3.6. ac/dc Conductivity

The AC conductivity of these samples was calculated from the values of dielectric constant and dielectric loss factor using the relation:

$$\sigma_{AC} = \omega\varepsilon'\varepsilon_o\tan\delta \tag{4}$$

where σ_{AC} is the AC conductivity, ω is the angular frequency, ε_o is the permittivity of free space, ε' is the dielectric constant and tanδ is the dielectric loss factor of the samples. Frequency dependent AC electrical conductivity, σ_{AC}, of $Mn_xNi_{1-x}Fe_2O_4$ NP's has been plotted in Fig. 9 for 20 °C and 120 °C measurements. From the plot, it is evident that the AC electrical conductivity is strictly frequency and temperature dependent.

The σ_{AC} slightly changes between 1 Hz and 10 kHz and above these frequencies; it increases fast with the increase in frequency. Also, by increasing the temperature, the σ_{AC} increases sharply as it can be seen from Fig. 9(b). The frequency dependent AC conductivity, σ_{AC} can be explained on the basis of Maxwell–Wagner two lattice model as elaborated below [19,39,40]. At lower frequency, the grain boundaries are more active, hence the hopping frequency of electrons between Fe^{3+} and Fe^{2+} ions is less. At higher frequencies, the conductive grains become more active by promoting the hopping of electrons between Fe^{3+} and Fe^{2+} ions therefore increasing the hopping frequency [19,27]. So we observe the increase in conductivity with the increase in frequency.

It is also observed that σ_{AC} increases with the increase in Mn concentration. Hopping of electrons between Fe^{2+} and Fe^{3+} ions on octahedral sites is responsible for conduction in ferrites [19,20,41]. Hole hopping between Ni^{2+} and Ni^{3+} ions on B site also contributes the conduction in ferrites. In $Mn_xNi_{1-x}Fe_2O_4$ system, the conduction depends upon the concentration of Mn ions on A site to the concentration of Ni ions on B site. The increase in AC conductivity by Mn concentration is due to the fact that Mn ions preferentially go to A sites and Ni ions to B sites. When the Ni^{2+} ions substituted with Mn^{2+} ions, Mn ions go to A sites and the concentration of Ni ions on B sites decreases. This favors the migration of the Fe ions from A sites to B sites. The probability of electron hopping, which is primary between Fe^{+2} and Fe^{+3} ions, is greater at the B sites due to smaller distances between the metallic ions at these sites. As a result of these, electron hopping between Fe^{2+} ions and Fe^{3+} ions responsible for the conduction increases. These types of changes have been observed for different studies [8,18–28].

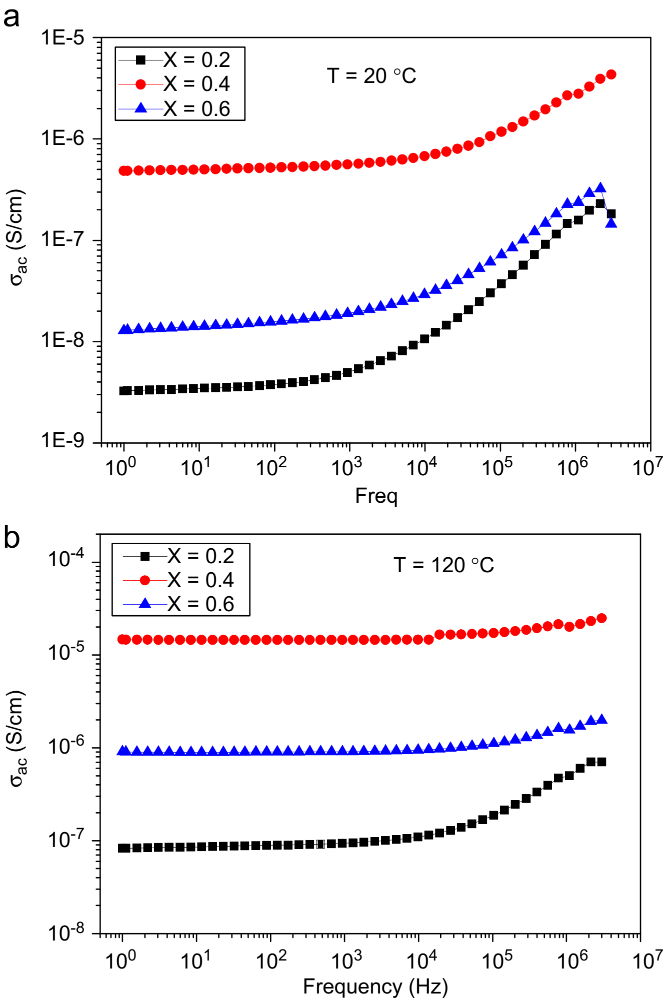

Fig. 9. Frequency dependent ac conductivity of the samples (a) at 20 °C and (b) at 120 °C.

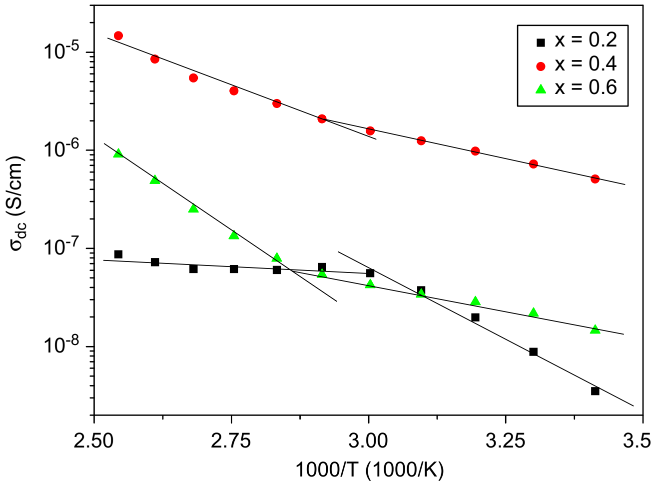

Fig. 10. Temperature dependent dc conductivity.

Temperature dependent direct current (dc) conductivity, σ_{dc}, of the samples which were derived from the plateau regions of the AC conductivity are plotted in Fig. 10. The dc conductivity σ_{dc}, of $Mn_xNi_{1-x}Fe_2O_4$ system increases with the increase in temperature according to the well-known Arrhenius relation (Eq. (5)) as expected for semiconductors:

$$\sigma = \sigma_0 \exp\left(-E_a/kT\right) \tag{5}$$

where E_a denotes the thermal activation energy of electrical conduction, σ_o is pre-exponential parameter which depends on the semiconductor nature and k is the Boltzmann's constant. As seen from dc conductivity graph, the conductivity of the samples is increasing with the temperature and obeys the thermally activated Arrhenius plot dc conductivity indicating the semiconducting nature of the samples. The increasing trend in the dc conductivity, σ_{dc}, with the temperature is due to the increase in drift mobility of the thermally activated charge carriers (electron and hole) according to hopping conduction mechanism [19,20].

The temperature dependence of σ_{dc} for all samples shows almost a straight line with two different activation energies. The line changes its slope at the Curie temperature Tc ~330–350 K, as was expected theoretically by

Kapse et al. [42]. It was reported that on passing through the Curie point a change in the gradient of the straight line (Fig. 10) must take place. The magnitude of this effect (gradient or slope) depends on the exchange interaction, which determines the Curie point, T_c [19,27]. The Curie temperature of the samples increases by the increase in Mn content and varies between 330 K and 350 K.

3.7. Dielectric properties

The dielectric constant (ε') for the compositions of $Mn_xNi_{1-x}Fe_2O_4$ NPs was calculated by the relation:

$$\varepsilon' = \frac{Cd}{\varepsilon_0 A} \qquad (6)$$

where C is the capacitance in Farad, d is the thickness of the pellets in m, A is the cross-sectional area of flat surface of the pellets in m^2, and ε_o is the permittivity of free space. The variation of the dielectric constant with the frequency and temperature for the system of $Mn_xNi_{1-x}Fe_2O_4$ NP's, is shown in Fig. 11. From Fig. 11 it is clear that all the samples exhibit high dielectric constant at low frequency region and each sample have similar dielectric behavior, showing strong dielectric dispersion. Dielectric constant increases with concentration of manganese and temperature but it decreases with increasing frequency. The decrease in dielectric constant is rapid at low frequency region and approaches to frequency independent behavior at high frequency region. These types of behaviors confirm the thermally activated relaxation which is typical for Debye-like relaxation and refer to it as the Maxwell–Wagner relaxation. The overall dielectric behavior is similar to that observed in different ferrite samples [19,20,28,43–45].

The decrease of dielectric constant with the increase in frequency can be explained on the basis of interfacial polarization as predicted by Maxwell and Wagner for the homogeneous double structure which is also in agreement with the Koop's phenomenological theory [39,40,46]. According to Maxwell–Wagner model, the dielectric model of ferrites is assumed to be made up of two layers: the first layer is being a well conducting layer that consists of large ferrite grains and the other is being the poorly conducting grain boundaries. The conducting grains are found to be more effective at higher frequencies while poor conducting grain boundaries are more effective at low frequencies as found in different ferrites [19,20,27,28,42]. The polarization in ferrites is through a mechanism similar to the conduction process by electron exchange between Fe^{2+} and Fe^{3+}, the local displacement of electrons in the direction of the applied field occurs and these electrons determine the polarization. The polarization decreases by increasing the frequency and approaches to a constant value due to the electron exchange between Fe^{2+} and Fe^{3+} cannot follow the alternating field. This decreases the probability of electrons reaching the grain boundaries and polarization decreases. Previously, the large value of dielectric constant at lower frequency was attributed to the predominance of species like Fe^{2+} ions, oxygen vacancies, grain boundary defects, etc. [39]. The decrease in dielectric constant with frequency is expected because of the fact that any species contributing to polarizability is found to show lagging behind the applied field at higher and higher frequencies [28].

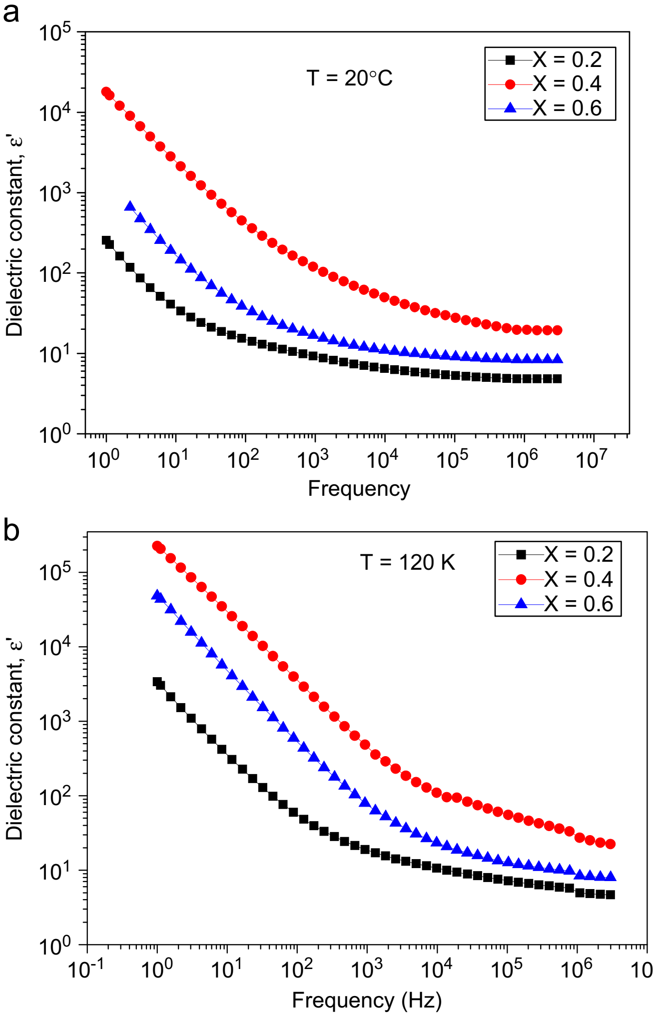

Fig. 11. Frequency dependence of dielectric constant (a) at 20 °C and at 120 °C.

Fig. 11 clearly shows the enhancement of dielectric permittivity at low frequencies. However, dielectric permittivity decreases at higher frequencies since the mobility of charge carriers is low at higher frequencies and cannot follow the alternation of applied ac electric field [47]. There are two mechanisms responsible for the permittivity dispersion for polycrystalline ferrites at higher frequency; they are ion and electron polarization [48]. The oxygen ion vacancies produced during the synthesis may also contribute to dielectric permittivity which is predominant at lower frequencies [49].

It can be seen that the sample shows the frequency-dependent phenomena i.e. the dielectric constant decreases with increasing frequency. This is a normal behavior observed in most of the ferrimagnetic materials, which may be due to the interfacial polarization as predicted by Maxwell–Wagner [19,20,39,40]. It can be explained on the basis that the solid is assumed as composed of well conducting grains separated by poorly conducting grain boundaries. Through hopping, the electrons reach the grain boundary and if the resistance of the grain boundary is high enough, the electrons pile up at the grain boundaries and produce polarization. The polarization in ferrites is through a mechanism similar to the conduction process. By electron exchange between Fe^{2+} and Fe^{3+}, the local displacement of electrons in the direction of the applied field occurs and these electrons determine the polarization. The polarization decreases with increasing frequency and then reaches a constant value due to the fact that beyond a certain frequency of external field, the electron exchange between Fe^{2+} and Fe^{3+} cannot follow the alternating field.

The method of preparation, cation distribution, grain size, sintering temperature, oxygen parameter, the ratio of Fe^{2+}/Fe^{3+} ions and oxygen anion vacancies in lattices influence the dielectric properties of nanoparticle ferrite materials [19,20,27,28,39,46]. The samples which assumed heterogeneous nature due to the individual grains influences the dielectric variation with frequency. Thus the dielectric behavior of the ferrites is attributed primarily to interfacial polarization resulting from their heterogeneous structure comprising low resistivity grains separated by high resistivity grain boundaries as suggested by Koops phenomenological dispersion theory [19,20,46]. The Fe^{2+} and Fe^{3+} ions present in ferrites contribute effectively to produce interfacial polarization. This is supported by the inverse proportionality between dielectric permittivity and resistivity as observed by various researchers [19,20,27,28,41–49].

4. Conclusion

In this study, manganese-substituted nickel ferrite nanoparticles of $Mn_xNi_{1-x}Fe_2O_4$ (x=0.2, 0.4, 0.6) have been prepared successfully by using PEG-assisted hydrothermal route. Well crystallized products were produced and the crystallite sizes were found between 6.5 and 11.0 nm by using line profile fitting of XRD pattern. SEM pictures show the size of NPs is at around 50 nm which is attributed to surfactant (PEG) on the surface of the NPs. The samples show superparamagnetic behavior at room temperature and ferromagnetic behavior with small coercivity at temperatures below the room temperature. The saturation magnetization, coercivity and conductivity are increased with the increase in Mn content. It is also observed that the dc conductivity increases with increasing temperature indicating the semiconducting nature of the samples. This behavior was attributed to the increase in drift mobility of the charge carriers with the temperature. While the dielectric constant was found to decrease with frequency, it was increasing with the temperature as observed in semiconductors. High value of the dielectric constant and revealed sharply reduced dielectric loss in these nanomagnetic samples making them as good candidates for applications as inductive and capacitive materials in capacitors used in electronic devices like memory cards, computers and as well as microwave absorbers.

Acknowledgments

This work is supported by the Fatih University under BAP Grant no. P50010701 and P50020902–2.

References

[1] A.R. Shyam, R. Dwivedi, V.S. Reddy, K.V.R. Chary, R. Prasad, Vapour phase methylation of pyridine with methanol over the $Zn_{1-x}Mn_xFe_2O_4$ (x=0, 0.25, 0.50, 0.75 and 1) ferrite system, Green Chemistry 4 (2002) 558–561.

[2] N. Gupta, A. Verma, S.C. Kashyap, D.C. Dube, Microstructural, dielectric and magnetic behavior of spin deposited nanocrystalline nickel–zinc ferrite thin films for microwave applications, Journal of Magnetism and Magnetic Materials 308 (2007) 137–142.

[3] M.A. Gabal, S.S. Ata-Allah, Effect of diamagnetic substitution on the structural, electrical and magnetic properties of $CoFe_2O_4$, Materials Chemistry and Physics 85 (2004) 104–112.

[4] N. Kasapoğlu, A. Baykal, Y. Köseoğlu, M.S. Toprak, Microwave-assisted combustion synthesis of $CoFe_2O_4$ with urea and its magnetic characterization, Scripta Materialia 57 (2007) 441–444.

[5] Y. Köseoğlu, H. Kavas, Size and surface effects on magnetic properties of Fe_3O_4 nanoparticles, Journal of Nanoscience and Nanotechnology 8 (2008) 584–590.

[6] Y. Köseoğlu, H. Kavas, B. Aktaş, Surface effects on magnetic properties of superparamagnetic magnetite nanoparticles, Physica Status Solidi A 203 (2006) 1595–1601.

[7] J. Smith, H.P.J. Wijn, Ferrites: physical properties of ferromagnetic oxides in relation to their technical applications, Wiley, New York, 1959.

[8] Y. Köseoğlu, A. Baykal, F. Gözüak, H. Kavas, Structural and magnetic properties of $Co_xZn_{1-x}Fe_2O_4$ nanocrystals synthesized by microwave method, Polyhedron 28 (2009) 2887–2892.

[9] D. Carta, M.F. Casula, A. Falqui, D. Loche, G. Mountjoy, C. Sangregorio, A. Corrias, A structural and magnetic investigation of the inversion degree in ferrite nanocrystals MFe_2O_4 (M = Mn, Co, Ni), Journal of Physical Chemistry C 113 (2009) 8606–8615.

[10] J. Azadmanjiri, Structural and electromagnetic properties of Ni–Zn ferrites prepared by sol–gel combustion method, Materials Chemistry and Physics 109 (2008) 109–112.

[11] U. König, G. Chol, X-ray and neutron diffraction in ferrites of $Mn_xZn_{1-x}Fe_2O_4$ type, Journal of Applied Crystallography 1 (1968) 124–126.

[12] K.P. Chae, J.G. Lee, H.S. Kweon, Y.B. Lee, The crystallographic, magnetic properties of Al, Ti doped $CoFe_2O_4$ powders grown by sol–gel method, Journal of Magnetism and Magnetic Materials 283 (2004) 103–108.

[13] Y. Cheng, Y. Zheng, Y. Wang, F. Bao, Y. Qin, Synthesis and magnetic properties of nickel ferrite nano-octahedra, Journal of Solid State Chemistry 178 (2005) 2394–2397.

[14] J.M.D. Coey, Noncollinear spin arrangement in ultrafine ferrimagnetic crystallites, Physical Review Letters 27 (1971) 1140–1142.

[15] M. Sertkol, Y. Köseoğlu, A. Baykal, H. Kavas, M.S. Toprak, Synthesis and magnetic characterization of $Zn_{0.7}Ni_{0.3}Fe_2O_4$ nanoparticles via microwave-assisted combustion route, Journal of Magnetism and Magnetic Materials 322 (2010) 866–871, http://dx.doi.org/10.1016/j.jmmm.2009.11.018.

[16] R.H. Kodama, A.E. Berkowitz, E.J. McNiff Jr., S. Foner, Surface spin disorder in $NiFe_2O_4$ nanoparticles, Physical Review Letters 77 (1996) 394–397.

[17] L. Zhou, Y. Cui, Y. Hua, L. Yu, W. Jin, S. Feng, The magnetic properties of $Ni_{0.7}Mn_{0.3}Gd_xFe_{2-x}O_4$ ferrite, Materials Letters 60 (2006) 104.

[18] C. Venkataraju, G. Sathishkumar, K. Sivakumar, Effect of nickel on the electrical properties of nanostructured Mn–Zn ferrite, Journal of Alloys and Compounds 498 (2010) 203–206.

[19] Y. Köseoğlu, M. Bay, M. Tan, A. Baykal, H. Sözeri, R. Topkaya, N. Akdoğan, Magnetic and dielectric properties of $Mn_{0.2}Ni_{0.8}Fe_2O_4$ nanoparticles synthesized by PEG-assisted hydrothermal method, Journal of Nanoparticle Research 13 (2011) 2235–2244.

[20] M. Tan, Y. Köseoglu, F. Alan, E. Şentürk, Overlapping large polaron tunneling conductivity and giant dielectric constant in $Ni_{0.5}Zn_{0.5}Fe_{1.5}Cr_{0.5}O_4$ nanoparticles (NPs), Journal of Alloys and Compounds 509 (2011) 9399–9405.

[21] F. Gözüak, Y. Köseoğlu, A. Baykal, H. Kavas, Synthesis and characterization of $Co_xZn_{1-x}Fe_2O_4$ magnetic nanoparticles via a PEG-assisted route, Journal of Magnetism and Magnetic Materials 321 (2009) 2170–2177.

[22] B.D. Culllity, Elements of X-rays Diffraction, Addison-Wesley, Reading, 1956.

[23] Qiang-min Wei, Jian Biao Li, Yong Junchen, Cation distribution and infrared properties of Ni_xMn_{1-x} ferrites, Journal of Materials Science 36 (2001) 5115–5118.

[24] Abid Hussain, Tahir Abbas, Shahida B. Niazi, Preparation of $Ni_{1-x}Mn_xFe_2O_4$ ferrites by sol–gel method and study of their cation distribution, Ceramics International, http://dx.doi.org/10.1016/j.ceramint.2012.07.049, in press.

[25] Y. Köseoğlu, F. Alan, M. Tan, R. Yilgin, M. Öztürk, Low temperature hydrothermal synthesis and characterization of Mn doped cobalt ferrite nanoparticles, Ceramics International 38 (2012) 3625–3634.

[26] A. Radhe Shyam, R. Dwivedi, V.S. Reddy, K.V.R. Chary, R. Prasad, Vapour phase methylation of pyridine with methanol over the $Zn_{1-x}Mn_xFe_2O_4$ ($x=0$, 0.25, 0.50, 0.75 and 1) ferrite system, Green Chemistry 4 (2002) 558–561, http://dx.doi.org/10.1039/b207410a.

[27] M. Sertkol, Y. Köseoğlu, A. Baykal, H. Kavas, A. Bozkurt, M.S. Toprak, Microwave synthesis and characterization of Zn-doped nickel ferrite nanoparticles, Journal of Alloys and Compounds 486 (2009) 325–329, http://dx.doi.org/10.1016/j.jallcom.2009.06.128.

[28 I.H. Gul, A.Z. Abbasi, F. Amin, M. Anis-ur-Rehman, A. Maqsood, Structural, magnetic and electrical properties of $Co_{1-x}Zn_xFe_2O_4$ synthesized by co-precipitation method, Journal of Magnetism and Magnetic Materials 311 (2007) 494–499, http://dx.doi.org/10.1016/j.jmmm.2006.08.005.

[29] J. Liu, T. Xua, M. Gong, F. Yu, Fundamental studies of novel inorganic–organic charged zwitterionic hybrids: 4. New hybrid zwitterionic membranes prepared from polyethylene glycol (PEG) and silane coupling agent, Journal of Membrane Science 283 (2006) 190–200, http://dx.doi.org/10.1016/j.memsci.2006.06.027.

[30] Y. Köseoğlu, M.I.O. Oleiwi, R. Yilgin, A.N. Koçbay, Effect of chromium addition on the structural, morphological and magnetic properties of nano-crystalline cobalt ferrite system, Ceramics International 38 (2012) 6671–6676, http://dx.doi.org/10.1016/j.ceramint.2012.05.055.

[31] Y. Xiaotun, X. Lingge, N.S. Choon, C.S. Hardy, Magnetic and electrical properties of polypyrrole-coated γ-Fe_2O_3 nanocomposite particles, Nanotechnology 14 (2003) 624–629, http://dx.doi.org/10.1088/0957-4484/14/6/311.

[32] B. Unal, Z. Durmus, A. Baykal, H. Sözeri, M.S. Toprak, L. Alpsoy, l-Histidine coated iron oxide nanoparticles: synthesis, structural and conductivity characterization, Journal of Alloys and Compounds 505 (2010) 172–178, http://dx.doi.org/10.1016/j.jallcom.2010.06.022.

[33] Z. Durmus, H. Kavas, A. Baykal, H. Sozeri, L. Alpsoy, S.Ü. Celik, M.S. Toprak, Synthesis and characterization of l-carnosine coated iron oxide nanoparticles, Journal of Alloys and Compounds 509 (2011) 2555–2561, http://dx.doi.org/10.1016/j.jallcom.2010.11.088.

[34] G. Balaji, N.S. Gajbhiye, G. Wilde, J. Weissmüller, Magnetic properties of $MnFe_2O_4$ nanoparticles, Journal of Magnetism and Magnetic Materials 242–245 (2002) 617–620, http://dx.doi.org/10.1016/S0304-8853(01)01043-5.

[35] C. Upadhyay, H.C. Verma, V. Sathe, A.V. Pimpale, Effect of size and synthesis route on the magnetic properties of chemically prepared nanosize $ZnFe_2O_4$, Journal of Magnetism and Magnetic Materials 312 (2007) 271–279, http://dx.doi.org/10.1016/j.jmmm.2006.10.448.

[36] C.N. Chinnasamy, A. Narayanasamy, N. Ponpandian, K. Chattopadhyay, H. Guerault, J.-M. Greneche, Magnetic properties of nanostructured ferrimagnetic zinc ferrite, Journal of Physics 12 (2000) 7795–7806, http://dx.doi.org/10.1088/0953-8984/12/35/314.

[37] D.L. Pelecky, R.D. Rieke, Magnetic properties of nanostructured materials, Chemistry of Materials 8 (1996) 1770–1783, http://dx.doi.org/10.1021/cm960077f.

[38] A. Sawatsky, F. van der Woude, A.H. Morrish, Cation distributions in octahedral and tetrahedral sites of the ferrimagnetic spinel $CoFe_2O_4$, Journal of Applied Physics 39 (1968) 1204–1206, http://dx.doi.org/10.1063/1.1656224.

[39] J.C. Maxwell, Electricity and Magnetism, vol. 1, Oxford University Press, Oxford, 1929 section 328.

[40] K.W. Wagner, Zur Theorie der Unvolkommenen Dielektrika, Annals of Physics 40 (1913) 817.

[41] R.C. Kambale, P.A. Shaikh, C.H. Bhosale, K.Y. Rajpure, Y.D. Kolekar, The effect of Mn substitution on the magnetic and dielectric properties of cobalt ferrite synthesized by an autocombustion route, Smart Materials and Structures 18 (2009) 115028.

[42] V.D. Kapse, S.A. Ghosh, F.C. Raghuwanshi, S.D. Kapse, U.S. Khandekar, Nanocrystalline $Ni_{0.6}Zn_{0.4}Fe_2O_4$: a novel semiconducting material for ethanol detection, Talanta 78 (2009) 19–25.

[43] M. Ajmal, A. Magsood, AC conductivity, density related and magnetic properties of $Ni_{1-x}Zn_xFe_2O_4$ ferrites with the variation of zinc concentration, Materials Letters 62 (2008) 2077.

[44] A.A. Birajdar, S.E. Shirsath, R.H. Kadam, S.M. Patange, D.R. Mane, A.R. Shitre, Frequency and temperature dependent electrical properties of $Ni_{0.7}Zn_{0.3}Cr_xFe_{2-x}O_4 (0 \le x \le 0.5)$, Ceramics International 38 (2012) 2963–2970.

[45] P.P. Hankare, V.T. Vader, N.M. Patil, S.D. Jadhav, U.B. Sankpal, M.R. Kadam, B.K. Chougule, N.S. Gajbhiye, Synthesis, characterization and studies on magnetic and electrical properties of Mg ferrite with Cr substitution, Materials Chemistry and Physics 113 (2009) 233–238.

[46] C.G. Koops, On the dispersion of resistivity and dielectric constant of some semiconductors at audio frequencies, Physical Review 83 (1951) 121–124 10.1103.

[47] A.M. Abdeen, Dielectric behavior in Ni–Zn ferrites, Journal of Magnetism and Magnetic Materials 192 (1999) 121–129, http://dx.doi.org/10.1016/S03048853(98)00324-2.

[48] G.C. Psarras, Hopping conductivity in polymer matrix-metal particles composites, Composites A 37 (2006) 1545–1553 http://dx.doi.org/10.1016/j.compositesa.2005.11.004.

[49] N. Ponpandian, A. Narayanasamy, Influence of grain size and structural changes on the electrical properties of nanocrystalline zinc ferrite, Journal of Applied physics 92 (5) (2002) 2770–2778 http://dx.doi.org/10.1063/1.1498883.